Eur. Phys. J. Plus (2024) 139:930
https://doi.org/10.1140/epjp/s13360-024-05752-5

THE EUROPEAN PHYSICAL JOURNAL PLUS

Regular Article

Impact of layer thickness on the efficiency of solar cells designed with zinc-based thin films produced by chemical bath deposition

Mehmet Fatih Gözükızıl[a]

Söğüt Vocational School, Bilecik Şeyh Edebali University, Söğüt, Bilecik 11600, Turkey

Received: 3 May 2024 / Accepted: 16 October 2024

Abstract Thin films of zinc-based materials were produced on glass substrates using the chemical bath deposition method. The study examined the effects of bath temperature and deposition time in the solution on the structural, surface, and optical properties of the deposited films. The results obtained led to the determination of the optimal deposition parameters, enabling the production of higher-quality zinc-based thin films. This research aimed to improve the understanding of the potential of zinc-based thin films and contribute to the development of higher-efficiency materials for applications in fields such as solar cells and optoelectronics. The solar cell layers in the GPVDM software were simulated by adding thin films of ZnO, ZnS, and ZnSe. The effect of layer thicknesses on the bandgap energies of zinc-based layers in solar cells was examined. It has been determined that zinc-based thin films have different bandgap energies and their optical properties vary. This phenomenon alters electron transport mobility and affects the layer thicknesses to achieve high efficiency in solar cells. Simultaneously, the influence of layer thicknesses on the efficiency of solar cells was investigated. When a zinc-based layer was used, it was found that the power conversion efficiency (PCE) reached up to 14 percent. The easy, economical production of thin films with desired characteristics will contribute to reducing the production cost and increasing the efficiency of solar cells, thus benefiting future solar energy technologies.

1 Introduction

The development and improvement of solar cells as an alternative to fossil fuels, which have limited resources and negative effects on the environment, are crucial for meeting the demand for clean and sustainable energy. The use of semiconductor thin films such as zinc oxide (ZnO), zinc sulfide (ZnS), and zinc selenide (ZnSe) in solar cells holds great potential. The energy band gaps of these materials, including ZnO, ZnS, and ZnSe, are important parameters that determine their optical and electronic properties [1]. ZnO typically has an energy band gap ranging from 3.2 to 3.4 eV [2, 3]. The energy band gap of ZnS usually falls between 3.5 and 3.8 eV [4–6], while ZnSe exhibits an energy band gap ranging from 2.4 to 2.8 eV [7, 8]. These band gaps determine the interaction of materials with photons and their electronic structures. A wider energy band gap enhances the ability of a material to absorb higher-energy photons and provides more efficient performance in optical applications [9–11]. Furthermore, the energy band gap also affects the semiconductor properties of the material and the degree of electronic conductivity [12]. ZnO exhibits high electron mobility and good conductivity, while ZnS and ZnSe may show lower conductivity compared to ZnO. The choice of material can influence the absorption spectrum of the cell and how it captures light. Optical properties encompass factors such as absorption coefficients, reflection, and transmission characteristics of the materials [13–17]. The use of ZnO, ZnS, and ZnSe thin films in solar cells has both advantages and disadvantages. The surface properties of these films, such as ZnO films typically having a flat and smooth surface, ZnS films composed of smaller and denser grains with a potentially rough surface, and ZnSe films characterized by large and irregular grains with a rough surface, may vary. These differences can be attributed to variations in the material's crystal structure, growth methods, and processing conditions. Various techniques can be employed to produce ZnO, ZnS, and ZnSe thin films, including physical vapor deposition (PVD) [18], chemical vapor deposition (CVD) [19], liquid phase deposition (LPD) [20], atomic layer deposition (ALD) [21, 22], and electrochemical deposition (ECD) [23]. PVD involves evaporating the material under vacuum and depositing it onto a substrate [24, 25], while CVD forms films through chemical reactions of reactive gases [26, 27]. LPD works by depositing material ions from a solution onto the substrate [28, 29], while ALD is an alternative technique where layers are deposited using alternating reactive gases [30]. ECD is a film growth process based on electrochemical reactions [31]. These methods allow for the production of ZnO, ZnS, and ZnSe films with different properties, which can be chosen based on application requirements. Chemical bath deposition (CBD) is widely preferred for depositing ZnO, ZnS, and ZnSe thin films due to its advantages such as low cost, simple process steps [32], and enabling large film areas [33]. This study focuses on the materials,

[a] e-mail: fatih.gozukizil@bilecik.edu.tr (corresponding author)

Published online: 24 October 2024

process parameters, production, and structural, surface, and optical characterization of ZnO, ZnS, and ZnSe thin films using the CBD method. PANalytical Empyrean X-ray diffraction (XRD), ZEISS Supra 40VP field emission scanning electron microscope (FESEM), Bruker energy-dispersive X-ray (EDX) detector, and UV–Vis spectrophotometer PerkinElmer Lambda 25 are used for comparative analysis to determine the crystal structures, surface morphologies, and optical properties of the films. The potential use of these thin films in solar cells is also evaluated. Furthermore, the results obtained using the GPVDM simulation program and their effects on solar cell performance are discussed. This study aims to improve our understanding of the potential of ZnO, ZnS, and ZnSe thin films in photovoltaic technology and contribute to the development of more efficient solar cells in the future.

2 Material and method

The production process of ZnO films begins by preparing a solution of 0.15 M zinc nitrate hexahydrate ($Zn(NO_3)_2.6H_2O$), which is procured from Sigma-Aldrich. To ensure rapid and homogeneous dissolution of the solution, it is stirred using a magnetic stirrer for 15 min. Subsequently, the pH of the solution is adjusted to 10 by adding a 25% aqueous ammonia (NH_4OH) solution. This step renders the solution alkaline by generating hydroxide ions (OH^-) in acidic solutions. As a result, the zinc ions in the solution react with the hydroxide ions, leading to the precipitation of ZnO. Thus, the presence of zinc ions in the solution creates an appropriate environment for the formation of ZnO films. Additionally, the alkaline environment facilitates the deposition of ZnO and ensures the desired crystalline structure of the film. For the production of ZnSe films, the compounds zinc sulfate heptahydrate ($ZnSO_4.7H_2O$) and selenourea ($SeC(NH_2)_2$) are sourced from Sigma-Aldrich, while hydrazine hydrate (N_2H_5OH) and 2% aqueous ammonia (NH_4OH) are obtained from Merck. In the production process, equal volumes of 0.25 M zinc sulfate heptahydrate, 0.2 M selenourea, and 0.25 M hydrazine hydrate are dissolved in 100 mL of distilled water to prepare the initial compounds required for the formation of ZnSe films. The resulting solutions are then mixed together to obtain a homogeneous mixture. Elevating the pH to 10 is carried out to accelerate the reactions of zinc sulfate heptahydrate, selenourea, and hydrazine hydrate, promoting the precipitation of ZnSe films from the solution. In the case of ZnS film production, the compounds zinc acetate dihydrate ($Zn(CH_3COO)_2.2H_2O$), trisodium citrate ($Na_3C_6H_5O_7.2H_2O$), and thiourea (N_2SCH_4) are sourced from Sigma-Aldrich, and 25% aqueous ammonia (NH_4OH) is obtained from Merck. The initial step involves preparing 0.075 M zinc acetate dihydrate, 0.25 M trisodium citrate, and 0.5 M thiourea solutions in 100 mL of distilled water. This mixture provides the starting compounds necessary for the formation of ZnS films. Subsequently, controlled addition of 25% aqueous ammonia (NH_4OH) to the mixture generates hydroxide ions (OH^-) in the solution, raising the pH to a constant value of 10. This process ensures that the pH of the solution reaches the desired level, creating a suitable environment for the formation of ZnS films. The chemical bath method is a process used to apply a coating with the desired properties onto the surface of materials. Figure 1 presents the schematic representation of the chemical bath process we have designed. Additionally, it is a method that requires careful implementation of factors such as the precise formulation of recipes for coating materials with the desired properties, temperature control throughout the process, homogeneous distribution of the solution, and maintaining stable pH values. This method is widely employed across various industries to enhance material properties and improve their performance.

Within the scope of the study, chemical solution preparation, cleaning of the substrate, dipping-withdrawal from the solution, and rinsing steps were applied, respectively. In the initial step of the process, suitable recipes were formulated in specified proportions to allow the material to be coated in the desired manner. After the solutions were prepared in beakers, they were placed in a bath in a larger beaker. The aim here is to keep the temperature of the coating solution constant at a certain degree. Two glass substrate samples with dimensions of 26 mm x 76 mm, which were pre-cleaned, were fixed to each other with the help of a holder and dipped in the solutions. In this way, it was aimed to cover only one surface of the base. They were kept in the solutions for 15 min, 30 min, 45 min, and 60 min. A magnetic stirrer heater was used to deposit the solution homogeneously on the substrate and to increase the temperature to the desired value. The magnetic fish in the coating solution was moved simultaneously with the magnetic spinner at the bottom of the beaker. The solution was applied at three different temperatures, 70 °C, 80 °C, and 90 °C, during the deposition process. Temperature control realized through temperature probe. In the coating process, the pH value of the solution is a critical parameter. The pH value was checked with a pH meter for an effective coating process. After the coated films were withdrawn from the bath, they were washed with distilled water to remove excess solution residues. This washing process ensured that the films had a pure and clean surface. Finally, the films were dried at room conditions. The chemical bath deposition (CBD) process on glass substrates has been conducted in a laboratory environment for controlled evaluation and analysis of the process. However, for the design of a thin film solar cell intended for industrial production, zinc-based films may be grown on alternative substrates such as ITO/coated glass, FTO/coated glass, or TiO_2, taking into consideration factors including the solar cell structure to be created, production method, and application requirements.

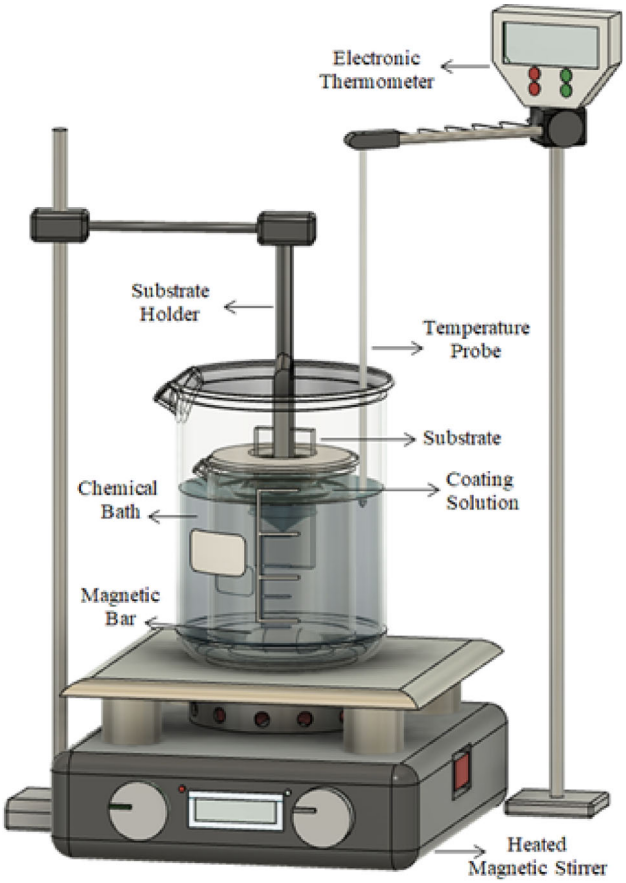

Fig. 1 Schematic illustration of chemical bath deposition method

3 Results and discussion

3.1 Deposition and characterization of zinc-based thin films

Within the scope of the study, the structural properties of ZnO, ZnS, and ZnSe films obtained at different bath temperatures of 70°C, 80°C, and 90°C, as well as at different deposition times of 15, 30, 45, and 60 min were investigated in detail by X-ray diffraction (XRD) method. The measurements were carried out in a PANalytical-Empyrean model X-ray machine using CuKα (λ =1.5405Å) beam at 2θ(20°-80°), 2°/min scan rate.

When the XRD spectra of ZnO films deposited at 70°C, 80°C, and 90°C bath temperatures were analyzed, as shown in Fig. 2(a), (010), (002), and (011) peaks of the hexagonal structure of ZnO (ASTM reference code: 98-005-7478) were observed at angles of 2θ= 31.72°, 34.35°, and 36.24°, respectively. Also, for 90°C, peaks (012), (110), (013), and (020) were observed at 2θ=47.26°, 56.50°, 62.80°, and 66.27°, respectively. The peak intensities increased in parallel with the increase in temperature. At 70°C, three peaks belonging to the hexagonal structure of ZnO were detected, while this increased to seven at 90°C. It was observed that the peak intensities reached the highest values at 90°C. According to these results, it is understood that the crystallinity of ZnS increases as the temperature rises. When the bath temperature exceeds 90°C, it is anticipated that the evaporation in the coating solution will increase, potentially leading to the concentration exceeding a tolerable level. For this reason, experiments were not conducted at temperatures above 90°C. Once it was understood that the best crystallinity occurred at 90 °C, time trials were carried out at the same temperature. XRD spectra of the ZnO films produced at the determined 90 °C bath temperature for 15, 30, 45, and 60 min in solution are given in Fig. 2(b). At 15th min, it was observed that no crystalline structure was formed, and ZnO structure started to form after 30th min. It was determined that the best crystallization occurred at 45th min. It was observed that the peak intensities decreased at 60th min with increasing deposition time and the structure started to deteriorate. The XRD spectra of zinc sulfide (ZnS) films fabricated at bath temperatures of 70°C, 80°C, and 90°C revealed the presence of peaks corresponding to the cubic ZnS (ASTM reference code: 98-016-2754), respectively. As shown in Fig. 2(c), the crystallinity of the ZnS structure is poor. It is also reported in the literature that the ZnS structure is a poor crystal [34, 35]. The films deposited at 70 °C bathing temperature did not show any peak formation. With the increase in temperature, the (111) peak of the ZnS structure started to appear at 2θ ≈27.31° and the (022) peak at 2θ ≈47.68° at 80 °C bathing temperature. When the bathing temperature was increased to 90 °C, the (113) peak was observed at 2θ ≈57.87° in addition to the other two peaks. It was also found that the intensities of the peaks formed in the film deposited at 90

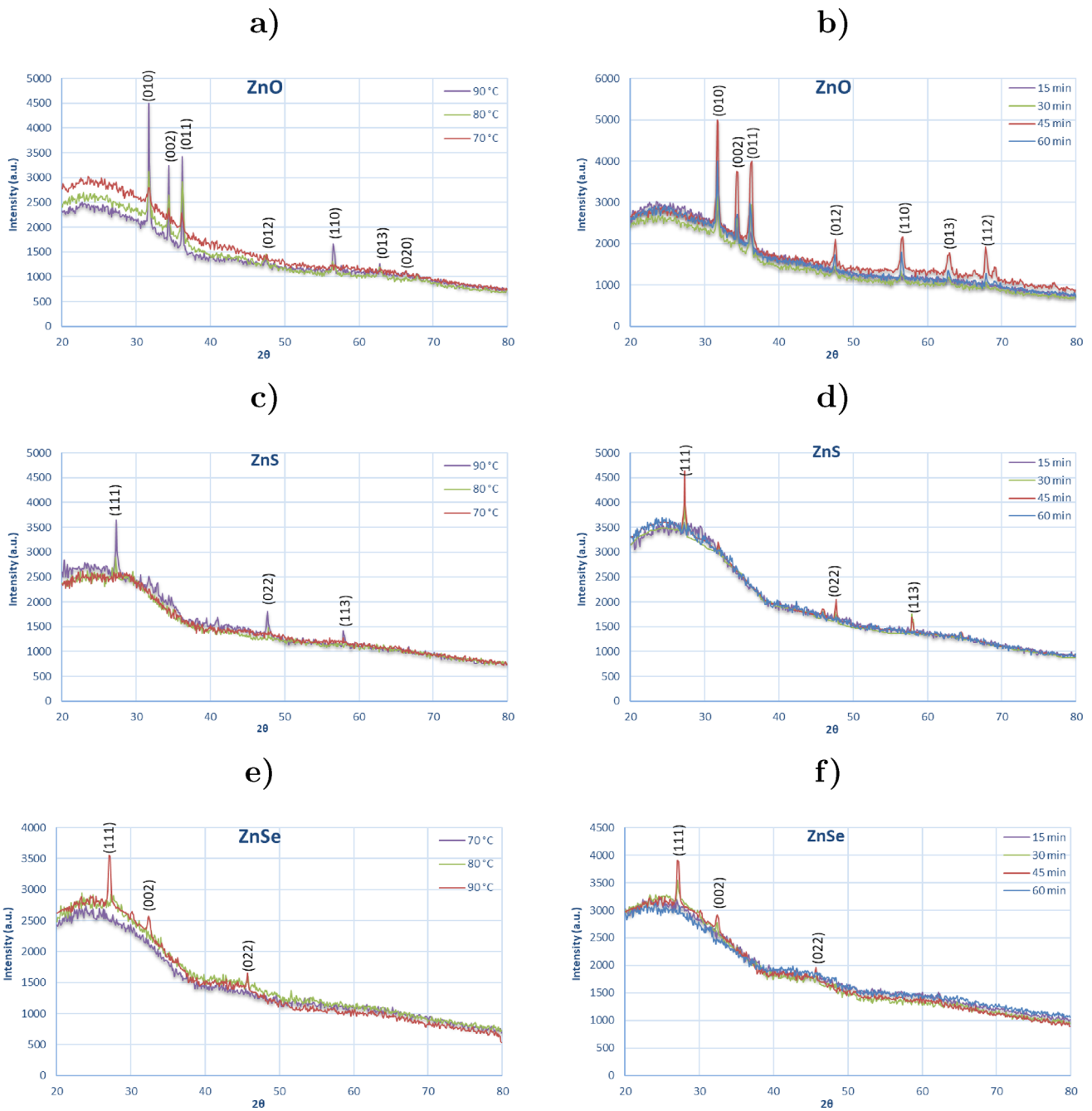

Fig. 2 XRD analysis spectra of zinc-based thin films at different temperatures and deposition times ZnO thin films **(a)**at different temperatures**(b)**at different deposition times ZnS thin films **(c)** at different temperatures **(d)** at different deposition times ZnSe thin films **(e)** at different temperatures **(f)** at different deposition times

°C bathing temperature were larger than the peak intensities of the other series. The peak intensities were also found to increase as the bathing temperature increased. The XRD spectra of ZnS films produced at 90°C bathing temperature for four different bathing durations (15, 30, 45, and 60 mins) are shown in Fig. 2(d). It was observed that the peak intensity gradually improved after the 30th minute, reaching its highest value at the 45th minute, and then diminishing toward the 60th minute. Therefore, a 45-minute duration was determined as the optimal time for operation at the ideal working temperature of 90°C. The XRD spectra of zinc selenide (ZnSe) films fabricated at bath temperatures of 70°C, 80°C, and 90°C revealed the presence of peaks corresponding to the cubic ZnSe (ASTM reference code: 98-004-1983), respectively. As shown in Fig. 2(e), the crystallinity of the ZnSe structure is poor. The poor crystallinity of the ZnSe structure has also been reported in the literature [36]. The films deposited at 70 °C and 80 °C bathing temperatures showed no peak formation. When the deposition temperature was increased to 90 °C, peaks at $2\theta \approx 28.65°$

(111), $2\theta \approx 33.20°$ (002), and $2\theta \approx 47.66°$ (022) were observed in addition to the other two peaks (113). It was determined that crystallization occurred in the film deposited at 90 °C bathing temperature. When the XRD spectrum in Fig. 2(f) of ZnS deposited as a thin film for 15, 30, 45, and 60 min was examined, three peaks were observed. ZnS with a cubic structure showed poor crystalline properties. The peaks are at 2θ angles 28.65°, 33.20°, and 47.66° for the (111), (002), and (022) planes, respectively, as depicted. At 15th min deposition time, no peak formation was observed. It was observed that the peak intensity gradually improved after the 30th minute, reaching its highest value at the 45th minute, and then diminishing toward the 60th minute. Therefore, 45-minute duration was determined as the optimal time for operation at the ideal working temperature of 90°C. SEM analyses were initially conducted on thin films of ZnO, ZnS, and ZnSe deposited on glass substrates using a ZEISS Supra 40VP field emission scanning electron microscope. The acquired SEM images were processed using image processing techniques such as contrast enhancement, noise reduction, and edge detection to create 3D models containing the topographical information of the surfaces. Subsequently, Gwyddion software was employed to transform these SEM images into AFM (atomic force microscope) images. This process led to the enhancement of surface images of ZnO, ZnS, and ZnSe thin films, and density maps were generated.

The SEM image in Fig. 3(a) reveals that the glass substrate samples coated with ZnO thin films exhibit a morphology resembling nano-rods, and these nano-rods appear to amalgamate into a flower-like structure. This observation aligns with the structure mentioned in the literature [37, 38]. According to the AFM images, it was ascertained that the coating thickness for ZnO films reached up to 700 nm at the apexes of the nano-rods, with an average thickness of approximately 500 nm.

When examining the surface images of the ZnS thin films in Fig. 3(b), it is observed that the surface is created by nearly homogeneously distributed nanoparticles. Additionally, it is evident that there are very few accumulations and voids on the surface, to the extent that they can be disregarded, indicating a better adhesion of the nanoparticles to each other. When AFM images were examined, it was determined that in some areas, the coating thickness reached up to 600 nm, with an average thickness of approximately 400 nm. The average roughness and particle sizes of the ZnS thin film were obtained with the optimized parameters in this study. Although the average thickness is reported as 400 nm, as seen in AFM analysis, the surface roughness is homogeneous at the nanoscopic scale and no clustering or large voids are observed. Therefore, it is thought that the ZnS film is suitable for thin film cells and the surface roughness does not negatively affect the performance.

The surface images of the ZnSe thin films presented in Fig. 3(c) reveal the presence of nano-sized particles, along with the observation that these particles form clusters. It has been determined that these nanoparticles cover the entire surface and create regional accumulations. The coating thickness of ZnSe films has been determined to be an average of 600 nm from the AFM images.

When examining the AFM images, it was observed that the surface roughness was highest in ZnO and lowest in ZnS thin films. This variation in surface roughness is due to changes in the atoms that bond with zinc. Even though ZnO, ZnS, and ZnSe thin films were produced under the same growth conditions and surface cleanliness, one of the most important reasons for their different surface roughness is their crystal structures. The distinct crystal structure of each material affects the arrangement of bonds between atoms and the topographic features of the surfaces. ZnO has a wurtzite structure, while ZnS has a zinc blend structure. These differing structures also result in different surface roughness.

In conclusion, despite having the same processing conditions, the natural crystal structures of the materials are a significant factor in influencing surface roughness. Since the images were observed at the nanoscale, there are occasional small variations in accumulation in certain areas. However, when considering the average surface roughness, these variations do not pose a problem for measurement.

The RMS (root mean square) roughness value, expressed in nanometers, was determined by averaging the height differences across the entire surface or in specific sections. The surface roughness values of the coated thin films are provided in Table1

The elemental atomic percentage values of the films have been obtained using an energy-dispersive X-ray spectrometer (EDX) detector and are presented in Table 2. Based on the atomic percentage values in the table, it can be observed that the coatings have been formed on the surface as desired.

The absorption spectra of the deposited thin films were collected within the wavelength range of 300–1000 nm. Figure 4(a) provides a comparative representation of the room temperature fundamental absorption spectra of ZnO, ZnS, and ZnSe. Figure 4(b) provides a comparative presentation of the optical transmittance spectra for all the series. In the visible region (400–800 nm), it was observed that ZnS exhibited a lower transmittance, while ZnO and ZnSe displayed values that were closer to each other. The comparative graph of $(\alpha h\mu)^2$ plotted against $(h\mu)$ for ZnO, ZnS, and ZnSe thin films is presented in Fig. 4(c). The values for the bandgap energy determined by the intersection of the linear part of the graph with the $h\mu$ axis are consistent with the eV values found in the literature [39–43].

3.2 Solar cell modeling and simulation method

The schematic representation of the simulated solar cell is shown in Fig. 5. This includes the arrangement and placement of the layers in solar cells according to their energy levels. Within the scope of this study, solar cells composed of ITO (indium tin oxide)/PEDOT:PSS (poly(3,4-ethylenedioxythiophene) polystyrene sulfonate)/P3HT:PCBM/ZnO (zinc oxide)/Al (aluminum) layers were designed. As an alternative layer, ZnS and ZnSe were utilized for the designed solar cells. Different layer thicknesses were investigated for their effects on power conversion efficiency (PCE). Initially, through preliminary experiments and literature research, the layer thicknesses were determined as 100 nm for ITO, PEDOT:PSS, Al layers, and 220 nm for P3HT:PCBM [44–46].

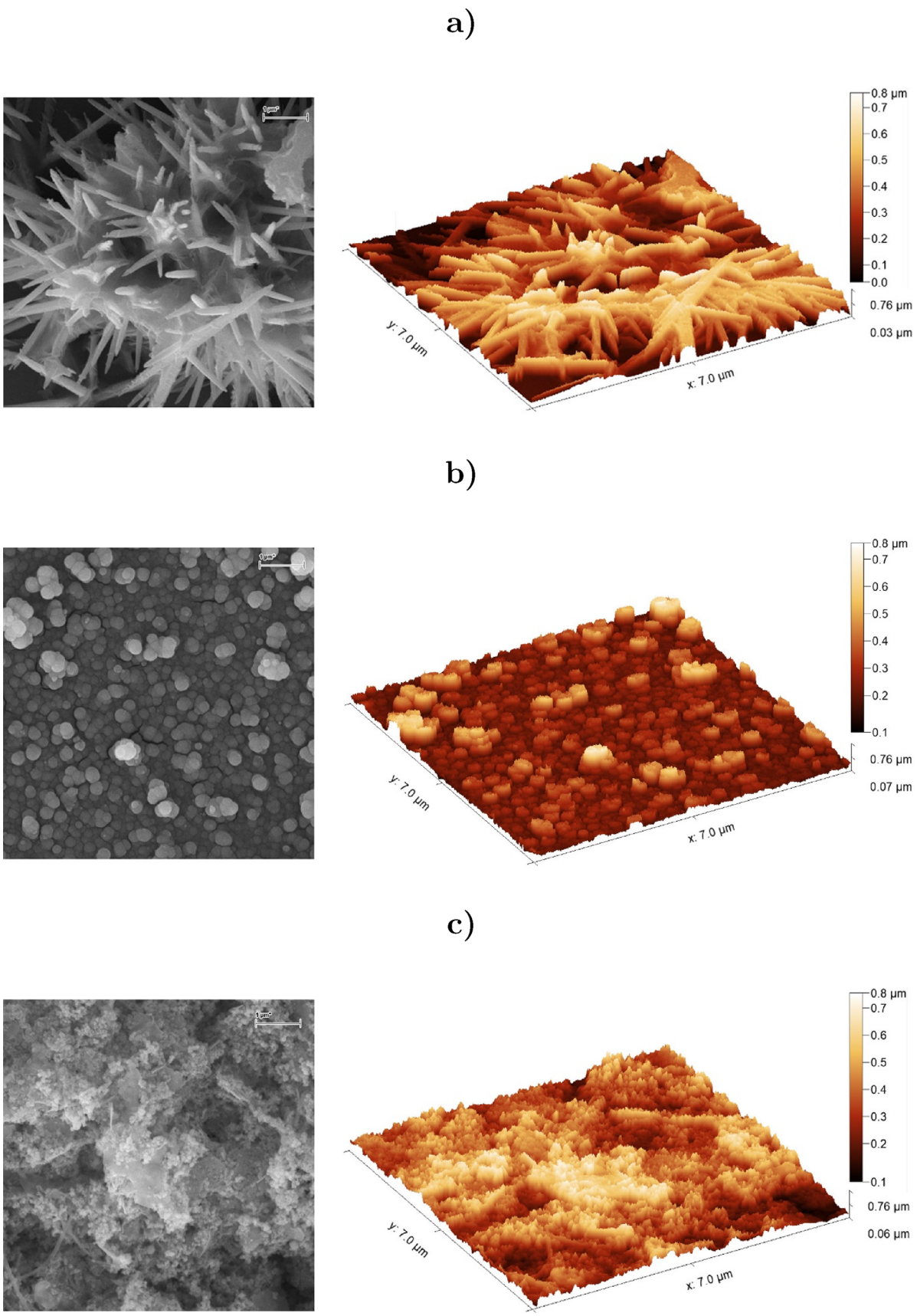

Fig. 3 SEM images of thin films and AFM images converted with Gwyddion software **(a)**Images of ZnO thin films **(b)** Images of ZnS thin films **(c)** Images of ZnSe thin films

Table 1 Roughness values of thin films

Coating material	ZnO	ZnS	ZnSe
RMS roughness (nm)	146,1	90,11	116,3
mean (nm)	124,1	67,63	94,2

Table 2 EDX results of thin films

	ZnO		ZnS		ZnSe	
Element	Zn	O	Zn	S	Zn	Se
Atomic (%)	60.84	39.16	61.72	38.28	50.31	49.69

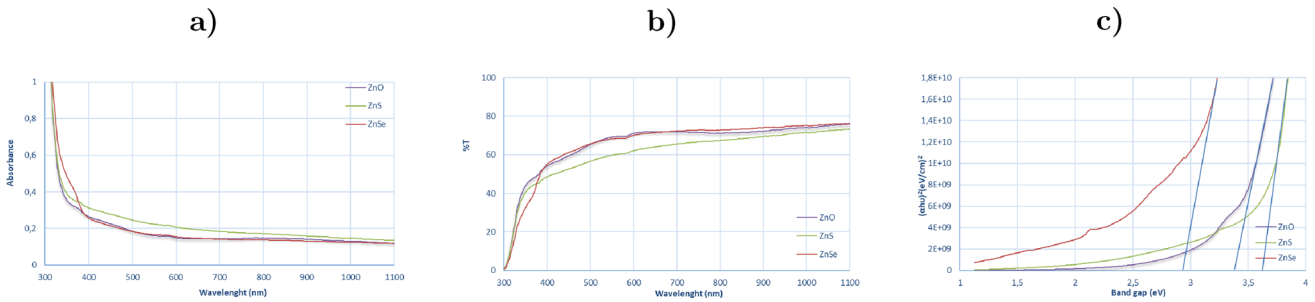

Fig. 4 **(a)** Absorption spectra of thin films **(b)** The optical transmittance spectra of thin films **(c)**The energy band gap of thin films

Solar cells were designed using GPVDM (General-purpose Photovoltaic Device Model) software to determine photovoltaic parameters and to compare the effect of thickness on these photovoltaic parameters. Solar cell performance tests were conducted at 300 K temperature and under 1 sun illumination with the AM 1.5G spectrum, taking into account the real atmospheric reflections of sunlight and its spectral distribution. The data obtained from the software were subsequently analyzed. Adsorption, optical transmittance, and energy band gap data obtained through optical characterization for ZnO, ZnS, and ZnSe were input into the GPVDM simulation program to create a new material. According to the specified plan, ZnO, ZnS, and ZnSe layers were defined as new materials and integrated separately. Dependent on the thickness of the placed layers, $V_{o\ c}$(open-circuit voltage), $J_{s\ c}$ (short-circuit current), and fill factor parameters were determined using simulation software. Based on these data, $P_{m\ a\ x}$ (maximum power output) values were calculated. The impact of layer thickness on photovoltaic conversion efficiency (PCE) was examined.

3.2.1 Simulation of solar cells and determination of photovoltaicparameters by adding zinc-based thin film layers

The photovoltaic parameters of the designed solar cells were determined by varying the ZnO, ZnS, and ZnSe layer thicknesses in the range of 100–1000 nm within the initially specified layer configurations. In Fig. 6(a)(b)(c), the effects of the thicknesses of ZnO, ZnS, and ZnSe layers added to the solar cell on the Voc, Jsc, and fill factor values are provided, respectively.

When the simulation data were analyzed in detail, it was determined that the optimal thickness of the ZnO layer for ITO/PEDOT:PSS/P3HT:PCBM/ZnO/Al solar cells was 500 nm. This value was determined as the optimal layer thickness to maximize energy conversion efficiency (PCE). Following the determination of the optimal ZnO thickness, experiments were carried out with a more detailed approach. The thickness of the P3HT:PCBM layer was varied between 100 and 500 nm, and then the thickness of the PEDOT:PSS layer was also adjusted within the same range. These experiments aimed to understand how different thicknesses of these two layers affect the performance of the solar cell. Analysis of the data revealed that the optimum thickness of the ZnS layer to obtain the best photovoltaic parameters was 600 nm. The ZnS layer thickness was kept constant at this value, and subsequent experiments were conducted to vary the thickness of the PEDOT:PSS and P3HT:PCBM layers, respectively. When investigating the effect of ZnSe layer thickness on the photovoltaic parameters of the solar cell, it was found that the optimal thickness of the ZnSe active layer is 400 nm. It was observed that values significantly decreased when the layer thickness exceeded 500 nm. The ZnO layer thickness was kept constant at 400 nm, and then, the thicknesses of the PEDOT: PSS and P3HT: PCBM layers were varied to determine their effects on the solar cells. In solar cells with added zinc-based thin film layers, the individual effects of PEDOT:PSS layer thicknesses on the photovoltaic parameters are provided in 6(d)(e)(f), respectively. Similarly, the effects of P3HT:PCBM layer thicknesses on the photovoltaic parameters are given in 6(g)(h)(i), respectively.

The detailed analysis of photovoltaic parameters presented in 6clearly demonstrates the effects of the thicknesses of the zinc-based thin film layer, as well as the P3HT:PCBM and PEDOT:PSS layers, on the efficiency of the solar cell. Additionally, the effects of layer thicknesses on the efficiency of solar cells with added ZnO, ZnS, and ZnSe layers are shown in 7(a)(b)(c), respectively.

The detailed analysis of photovoltaic parameters reveals the impact of ZnO, P3HT:PCBM, and PEDOT:PSS layer thicknesses PCE. According to the simulation results, we determined the most appropriate thickness values for the solar cell by examining the

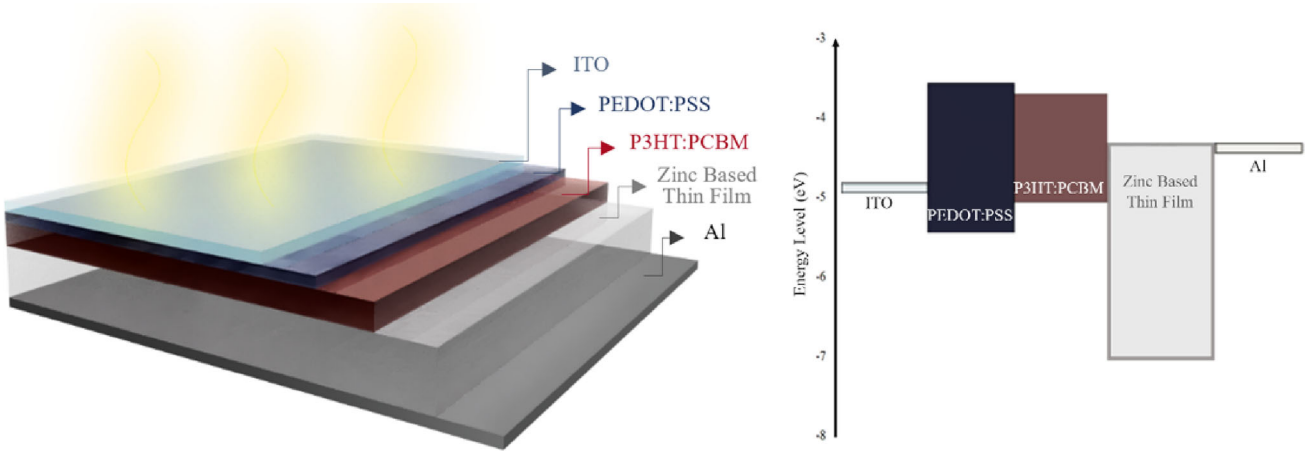

Fig. 5 Schematic representation of the simulated solar cell and layer energy levels

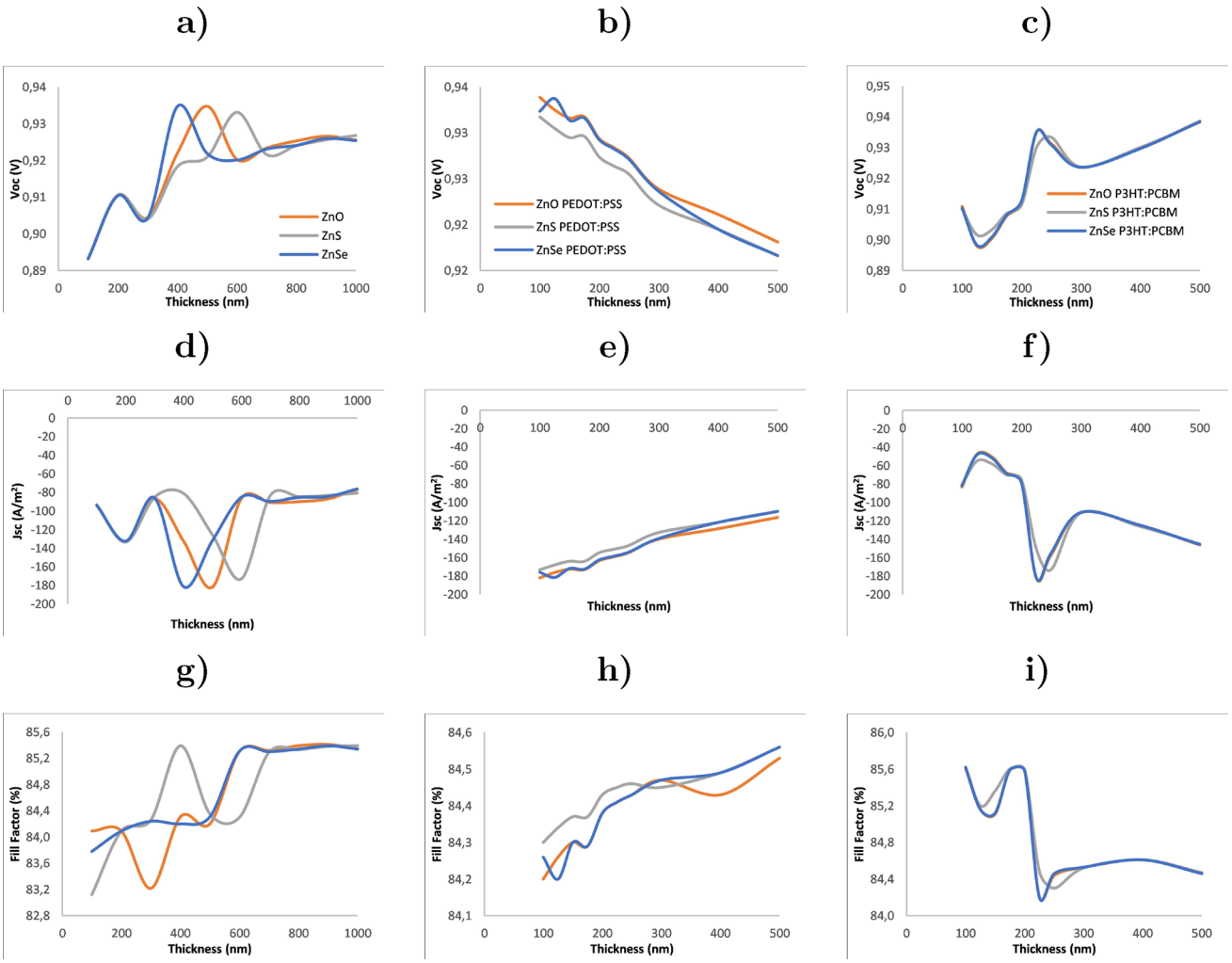

Fig. 6 hl V_{oc} (V) Values of **(a)** ZnO, ZnS, and ZnSe layers of various thicknesses**(b)** PEDOT:PSS layers of various thicknesses **(c)** P3HT:PCBM layers of various thicknesses $J_s c$ (A/m^2) Values of **(d)** ZnO, ZnS, and ZnSe layers of various thicknesses **(e)** PEDOT:PSS layers of various thicknesses **(f)** P3HT:PCBM layers of various thicknesses fill factor (%) Values of **(g)** ZnO, ZnS, and ZnSe layers of various thicknesses **(h)** PEDOT:PSS layers of various thicknesses **(i)** P3HT:PCBM layers of various thicknesses

effects of layer thicknesses on the performance of the solar cell. The ideal ZnO layer thickness was found to be 500 nm. While the optimum thickness for the PEDOT:PSS layer was 100 nm, it was determined as 225 nm for the P3HT:PCBM layer. These values

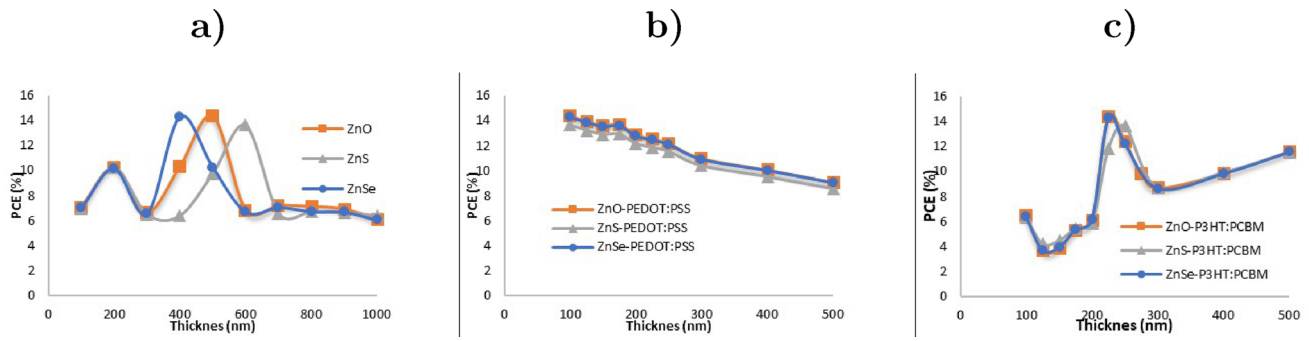

Fig. 7 Comparison of the effect of the thickness of **(a)** ZnO, ZnS, and ZnSe layers **(b)** PEDOT:PSS layers **(c)** P3HT:PCBM layers on PCE

were obtained through detailed analysis with the aim of maximizing the PCE of the solar cell. Taking these values into account can potentially ensure that the solar cell operates at peak efficiency. It was found that the initial 100 nm increase in the thickness of the PEDOT:PSS layer significantly reduced the PCE of the solar cell with added ZnS layer. It was also observed that the PCE value was high at P3HT:PCBM layer thicknesses of 225 nm and 250 nm, but when these thicknesses were further increased, the PCE value started to decrease again. Based on the analysis of the data collected, the optimal thicknesses for the PEDOT:PSS layer, ZnS layer, and P3HT:PCBM active layer were determined to be 100 nm, 600 nm, and 250 nm, respectively. In cells with added ZnSe layer, an increase in the thickness of the PEDOT:PSS layer starting from 125 nm led to a decrease in efficiency, and a more significant decrease was observed after reaching 300 nm. Additionally, it was determined that the highest efficiency value occurred when the thickness of the P3HT:PCBM layer was 225 nm and decreased after reaching 250 nm. Optimal thicknesses were observed to be 400 nm for ZnSe, 125 nm for PEDOT:PSS, and 225 nm for P3HT:PCBM layers, respectively.

4 Conclusion

Using a chemical bath method, zinc-based thin films have been successfully deposited at low cost and with repeatability, without the need for vacuum or high temperatures. During this process, the risk of reducing the substrate material's strength and altering its physical properties has been minimized. In the experiments conducted for the deposition of zinc-based thin films, the pH was maintained at 10, and different bath temperatures and deposition times were tested. The XRD results of all the tested samples were compared. As a result, the ideal bath temperature was determined to be 90°C, and the ideal deposition time was established as 45 min. This led to an improvement in the quality of zinc films and made the production process more efficient. The SEM images obtained revealed that ZnO thin films were formed in the shape of nano-rods on the surface, while ZnS and ZnSe films were formed in the shape of nanoparticles. The AFM images were used to calculate the average coating thickness, which was found to be 500 nm for ZnO films, 400 nm for ZnS films, and 600 nm for ZnSe films. Because ZnO films are composed of nano-rods and ZnSe films are made up of smaller nanoparticles, the surface roughness was found to be higher in ZnSe films compared to ZnS films. The optical properties of thin films were characterized, and their bandgap energies were calculated for use in solar cell simulations. The produced zinc-based thin films were found to possess unique photovoltaic and electrical properties as well as varying surface roughness. Their suitability for use as a layer in solar cells was tested. The solar cells formed in the ITO/PEDOT:PSS/P3HT:PCBM/Al layers were aimed to be improved in efficiency by adding zinc-based layers after the P3HT:PCBM layer. Layer thicknesses were varied to study their effects on efficiency. Prior to the addition of zinc-based layers, the photovoltaic parameters of ITO/PEDOT:PSS/P3HT:PCBM/Al layered solar cells were determined as follows: fill factor 0.668274, $V_{o\ c}$ 0.603952 V, and $J_s\ c$ −155.465 A/m^2. The energy conversion efficiency (PCE) was calculated to be 4.46%. When ideal thicknesses of ZnO, ZnS, and ZnSe were incorporated as layers in the solar cell, PCE was calculated to be 14.3%, 13.5%, and 14.2%, respectively. The observed 14% efficiency indicates significant potential for further improvements and optimizations. It is possible to enhance efficiency through improvements in parameters such as band structure alignment between p-type and n-type layers, electron and hole transport, minimization of interface transition resistances, and optimization of layer thicknesses. It was observed that the zinc-based layers significantly improved the efficiency of the solar cell. The increase in layer thicknesses resulted in a decrease in transmission (%T) values, consequently leading to an increase in the bandgap energies. The changing bandgap energies of zinc-based thin films have led to variations in electron transport mobility, consequently affecting both their photovoltaic and electrical properties. Therefore, the ideal layer thicknesses have been determined as 400 nm for ZnS with a bandgap energy of 2.92 eV, 500 nm for ZnO with a bandgap energy of 3.35 eV, and 600 nm for ZnSe with a bandgap energy of 3.54 eV. It was observed that layer thicknesses have a direct impact on the bandgap energies, and an increase

in the bandgap energy leads to an increase in layer thickness. Thus, it was revealed that the properties of zinc-based films can be easily modified to enhance the efficiency of solar cells.

Author contributions M.F.G. contributed to conceptualization, framing, methodology, formal analysis, validation, writing, review and editing, and visualization.

Funding This research was conducted without any funding.

Data Availability Statement This manuscript has associated data in a data repository. [Authors' comment: All data included in this manuscript are available upon request by contacting the corresponding author].

Declaration

Conflict of interest All authors declare no conflict of interest.

References

1. M. Nebi, D. Peker, S. Temel, Deposition of co doped tio2 films using sol gel spin coating technique and investigation of band gap. In: AIP Conference Proceedings, vol. 1935 (2018). AIP Publishing
2. M.F. Gozukizil, S. Temel, N. Ozbay, Some physical properties of czo thin films produced by a novel magnetic spin coating technique. Sigma Journal of Engineering and Natural Sciences **38**(2), 955–960 (2020)
3. M.F. Gozukizil, S. Temel, N. Ozbay, Production and characterization of al-doped zno thin films with sol-gel magnetic spin coating technique. Sakarya University Journal of Science **24**(1), 172–177 (2020)
4. S.S.A. Shah, S.U. Awan, S. Zainab, H. Tariq, M.B. Riaz, A. Ul-Haq, N. Shahzad, N. Iqbal, N to p-type transition with narrowing optical bandgap and increasing carrier concentration of spin coated cu doped zns thin films for optoelectronic applications. Optical Materials **141**, 113816 (2023)
5. M. Banuprakash, R. Bairy, M. Murari, Linear and third-order nonlinear optical properties of spray pyrolysis deposited mn doped zns nanostructured thin films for optoelectronic device applications. Materials Today: Proceedings (2023)
6. V. Ashith, S.N. Moger, Influence of magnesium dopant on zns thin films by low-cost chemical bath deposition technique. Optik **284**, 170934 (2023)
7. R. Khalfi, D. Talantikite-Touati, A. Tounsi, A. Souici, F.A. Merzeg, A. Azizi, Effect of manganese doping on the structural, morphological and optical properties of zinc selenide thin films prepared by chemical bath deposition method. Applied Physics A **129**(3), 231 (2023)
8. P. Gupta, R.G. Solanki, P. Patel, K. Sujata, R. Kumar, A. Pandit, Enhanced antibacterial and photoluminescence activities of znse nanostructures. ACS omega **8**(15), 13670–13679 (2023)
9. N. Shrivastav, S. Kashyap, J. Madan, A.K. Al-Mousoi, M.K. Mohammed, M.K. Hossain, R. Pandey, J. Ramanujam, Perovskite-cigs monolithic tandem solar cells with 29.7% efficiency: a numerical study. Energy & Fuels 37(4), 3083–3090 (2023)
10. A. Islam, S.H. Teo, M.T. Islam, E. Ahamed, M.S. Islam, A.G. Alsultan, H.M. Marwani, M.M. Rahman, A.M. Asiri, Y.H. Taufiq-Yap et al., Boosting biodiesel production over silicon heterojunction with visible light irradiation. Energy Conversion and Management **292**, 117435 (2023)
11. N. Shrivastav, S. Kashyap, J. Madan, M.K. Mohammed, M.K. Hossain, R. Pandey, An efficient all-perovskite two terminal monolithic tandem solar cell with improved photovoltaic parameters: A theoretical prospect. Optik **281**, 170821 (2023)
12. S. Li, A. Liu, Z. Yang, J. He, J. Wang, F. Liu, H. Lu, X. Yan, P. Sun, X. Liang et al., Room temperature gas sensor based on tin dioxide@ polyaniline nanocomposite assembled on flexible substrate: ppb-level detection of nh3. Sensors and Actuators B: Chemical **299**, 126970 (2019)
13. S.-S. Kong, W.-K. Liu, X.-X. Yu, Y.-L. Li, L.-Z. Yang, Y. Ma, X.-Y. Fang, Interlayer interaction mechanism and its regulation on optical properties of bilayer sicnss. Frontiers of Physics **18**(4), 43302 (2023)
14. C. Edet, E. Al, F. Ungan, N. Ali, M. Ramli, M. Asjad, Effects of the confinement potential parameters and optical intensity on the linear and nonlinear optical properties of spherical quantum dots. Results in Physics **44**, 106182 (2023)
15. K. Lakaal, D. Mazkad, M. Beraich, A. El Fatimy, M. Courel, L. Pérez, P. Díaz, D. Laroze, E. Feddi et al., First principles study on electronic and optical properties of cu2coges4 for photovoltaic conversion and photocatalytic applications. Materials Research Bulletin **164**, 112235 (2023)
16. K. Rodríguez-Magdaleno, F. Nava-Maldonado, E. Kasapoglu, M. Mora-Ramos, F. Ungan, J. Martínez-Orozco, Nonlinear absorption coefficient and relative refractive index change for konwent potential quantum well as a function of intense laser field effect. Physica E: Low-dimensional Systems and Nanostructures **148**, 115618 (2023)
17. Z. Abbas, K. Fatima, I. Gorczyca, S.H.A. Jaffery, A. Ali, M. Irfan, H.H. Raza, H. Algarni, S. Muhammad, H. Teisseyre et al., First-principles calculations to investigate electronic, optical, and thermoelectric properties of na2gex3 (x= s, se, te) for energy applications. Materials Science in Semiconductor Processing **154**, 107206 (2023)
18. M.A. Mayimele, J.N. Fru, J.S. Nyarige, M. Diale, Sequential physical vapor deposited methylammonium lead tri-iodide perovskites on fto and ito modified zinc oxide nanorods for perovskite solar cells. Physica B: Condensed Matter **625**, 413462 (2022)
19. Y. Kurimoto, D. Kobayashi, N. Asou, T. Okamoto, Formation and characterization of zns and cdzns films using open-air chemical vapor deposition for buffer layers of compound semiconductor solar cells. Japanese Journal of Applied Physics 62(SK), 1048 (2023)
20. C.-F. Yen, Y.-Y. Huang, S.-H. Tsao, H.-C. Hsu, Analysis of electrical properties in mos structure with a low surface roughness al 2 o 3-doped zno film as gate oxide, 102–106 (2022). IEEE
21. Z. Starowicz, A. Zieba, J. Ostapko, M. Wlazlo, G. Kolodziej, M.J. Szczerba, G. Putynkowski, R.P. Socha, Synthesis and characterization of al-doped zno and al/f co-doped zno thin films prepared by atomic layer deposition. Materials Science and Engineering: B **292**, 116405 (2023)
22. C. Hong, M. Kim, J.-G. Lee, Q. Shao, H.-S. Lee, H.-H. Park, et al. Research of si-zno thin-film transistors deposited by atomic layer deposition. International Journal of Energy Research **2023** (2023)
23. I. Demidenko, V. Ishimov, Electrochemical deposition of zinc sulfide from a na2so3-based electrolyte. Surface Engineering and Applied Electrochemistry **58**(2), 109–115 (2022)
24. M. Vorobyova, F. Biffoli, W. Giurlani, S.M. Martinuzzi, M. Linser, A. Caneschi, M. Innocenti, Pvd for decorative applications: A review. Materials **16**(14), 4919 (2023)
25. T.C. Senocak, Characterization and performance of tantalum-tungsten based coatings deposited on cp-ti substrates by pvd technique. Materials Today Communications **37**, 107091 (2023)

26. S. Li, X. Wang, H. Li, J. Fang, D. Wang, G. Xie, D. Lin, S. He, L. Qiu, Low-temperature chemical bath deposition of conformal and compact niox for scalable and efficient perovskite solar modules. Small **19**(34), 2301110 (2023)
27. Y. Hoshikawa, Coating nanoporous ceramics with carbon by a cvd method and analysis of their characteristics as electrochemical devices. Carbon Reports **2**(3), 130–145 (2023)
28. K. Saito, N. Matsushita, Y. Kubota, Ceo2 coatings on conductive polyethylene foams via gas-assisted liquid phase deposition and their humidity sensor performance. Journal of the Ceramic Society of Japan **131**(8), 376–382 (2023)
29. M. Honda, T. Ochiai, P. Listiani, Y. Yamaguchi, Y. Ichikawa, Low-temperature synthesis of cu-doped anatase tio2 nanostructures via liquid phase deposition method for enhanced photocatalysis. Materials **16**(2), 639 (2023)
30. S. Yasmeen, S.W. Ryu, S.-H. Lee, H.-B.-R. Lee, Atomic layer deposition beyond thin film deposition technology. Advanced Materials Technologies **8**(20), 2200876 (2023)
31. T. Wang, L. Wang, Y. Chen, L. Zhu, M. Yang, S. Zhang, C. Niu, Y. Lv, Polyaniline films fabricated by pre-nucleation electrodeposition method with high electrochemical activity: Parameter optimization and analysis. Macromolecular Chemistry and Physics **225**(3), 2300333 (2024)
32. A.F. Abdulrahman, N. Abd-Alghafour, M.A. Almessiere, A high responsivity, fast response time of zno nanorods uv photodetector with annealing time process. Optical Materials **141**, 113869 (2023)
33. Q. Li, Y. Zhang, B. Ji, S. Zhang, R. Tu, Improvement of sic deposition uniformity in cvd reactor by showerhead with baffle. Journal of Crystal Growth **615**, 127255 (2023)
34. S. Sartale, B. Sankapal, M. Lux-Steiner, A. Ennaoui, Preparation of nanocrystalline zns by a new chemical bath deposition route. Thin Solid Films **480**, 168–172 (2005)
35. R. Zhang, B. Wang, H. Zhang, L. Wei, The structure and optical properties of the nanocrystalline zns films prepared by sulfurizing the as-deposited zno films. Applied surface science **241**(3–4), 435–441 (2005)
36. J. Ke, R. Zhang, P. Zhang, R. Yu, X. Cao, P. Kuang, B. Wang, Investigation on structural and optical properties of znse thin films prepared by selenization. Superlattices and Microstructures **156**, 106965 (2021)
37. D. Mani, S.S. Manoharan, G.J. Arputhavalli, G. Sriram, S. Jebasingh, A study on morphology dependent nanostructured zno thin films: An efficient gas sensing response for acetaldehyde. Inorganic Chemistry Communications **150**, 110471 (2023)
38. P. Rai, S. Raj, K.-J. Ko, K.-K. Park, Y.-T. Yu, Synthesis of flower-like zno microstructures for gas sensor applications. Sensors and Actuators B: Chemical **178**, 107–112 (2013)
39. S. Temel, Influence of deposition temperature on structural, morphological, and optical properties of zns thin films. Canadian Journal of Physics **96**(7), 826–830 (2018)
40. Z. Long, G. Yang, R. Shao, Z. Chen, Y. Liu, R. Liu, H. Zhong, The strain effects and interfacial defects of large znse/zns core/shell nanocrystals. Small, 2306602 (2023)
41. P.K. Narayanam, Efficient tunability of size and optical properties of reduced graphene oxide-zno composite nanocrystallites on solid substrates. Colloids and Surfaces A: Physicochemical and Engineering Aspects **665**, 131229 (2023)
42. S. Temel, M. Nebi, D. Peker, Optical band gap engineering of (mgo) x (zno) films deposited by sol-gel spin coating. Optoelectronics and Advanced Materials - Rapid Communications **12**, 76–79 (2018)
43. D. Peker, S. Temel, M. Nebi, Mg-doped zno films by sol-gel spin coating method. International Journal of Scientific and Technological Research **1**(1), 263–269 (2015)
44. C.S. Kundu, A. Adhikary, M.S. Ahsan, A. Rahaman, M.B. Hossain, A.D. Raha, S.A. Murad, F. Ahmed, Design and analysis of performance parameters for achieving high efficient ito/pedot: Pss/p3ht: Pcbm/al organic solar cell. Journal of Optics, 1–12 (2023)
45. J.H. Han, P. Sadhukhan, J.-M. Myoung, Highly flexible and stable green perovskite light-emitting diodes based on il-modified pedot: Pss film. Applied Surface Science **641**, 158493 (2023)
46. H.-L. Loi, J. Cao, C.-K. Liu, Y. Xu, M.G. Li, F. Yan, Highly sensitive broadband phototransistors based on gradient tin/lead mixed perovskites. Small **19**(3), 2205976 (2023)